nature materials

Supplementary information

For

Magnetoresistance governs apparent magnetic-field enhancements in water electrolysis

Vadim Ratvoskii[1,*], *Emma van der Minne*[1,*], *Florian Gossing*[2], *Jelle R. H. Ruiters*[1], *Iris C. G. van den Bosch*[1], *Michael Verhage*[3], *Daan H. Wielens*[1], *Jeffrey McCord*[2], *Gertjan Koster*[1], *Christoph Baeumer*[1,4]

[1] MESA+ Institute for Nanotechnology, Faculty of Science and Technology, University of Twente, Hallenweg 15, Enschede, 7522 NH, The Netherlands
[2] Department of Materials Science, Kiel University, Kaiserstraße 2, Kiel, 24143, Germany.
[3] Materials to Optoelectronic Devices (M2D), Departments of Applied Physics and Chemical Engineering and Chemistry, Eindhoven University of Technology, Helix Building, Eindhoven, 5600 MB, The Netherlands.
[4] Peter Gruenberg Institute – Electronic Materials (PGI-7), Forschungszentrum Juelich GmbH, Wilhelm-Johnen-Straße, Jülich, 52428, Germany

Correspondence
*these authors contributed equally
Corresponding authors: Vadim Ratovskii, Email:v.ratovskii@utwente.nl, Emma van der Minne, Email: e.vanderminne@utwente.nl & Christoph Baeumer. Email: c.baeumer@utwente.nl

Contents

S.1 Magnetic hysteresis of current-collector layers

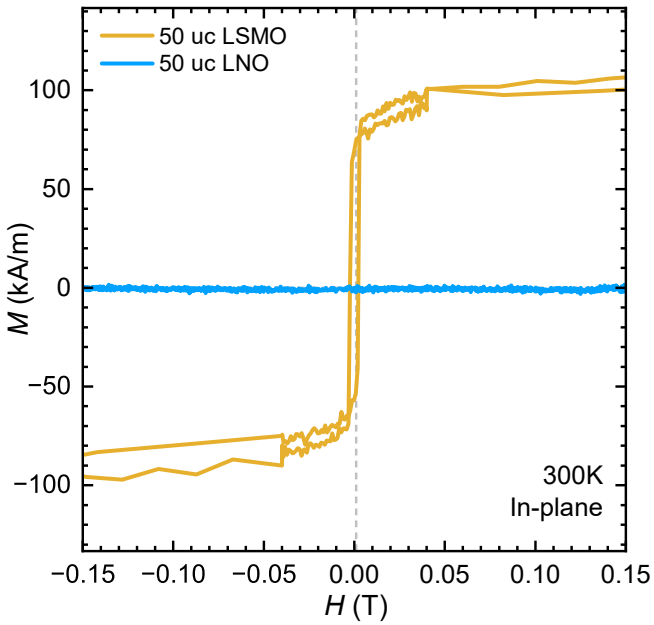

FIGURE S1 Magnetization hysteresis of representative current-collector layers measured at 300 K under an in-plane magnetic field. Linear diamagnetic or paramagnetic contributions from the substrate or the layers were substrated for all the samples. The $LaNiO_3$ (LNO) layer thickness was increased relative to the 12 unit cells used in the main text to achieve a volume comparable to that of the LSMO layer, enabling a more meaningful comparison.

Magnetic hysteresis loops of bare conductive layers of LSMO (50 uc) and LNO (50 uc) on STO reveal the anticipated magnetic behavior. While LSMO clearly shows ferromagnetic hysteresis loop at room temperature, the magnetization of LNO remains zero with applied magnetic field due to its paramagnetic nature and the subsequent removal of the diamagnetic or paramagnetic contributions from the substrate or the layers for all the samples during the post-analysis stage.

S.2 Transmission Electron Microscopy analysis of CFO-based multilayers

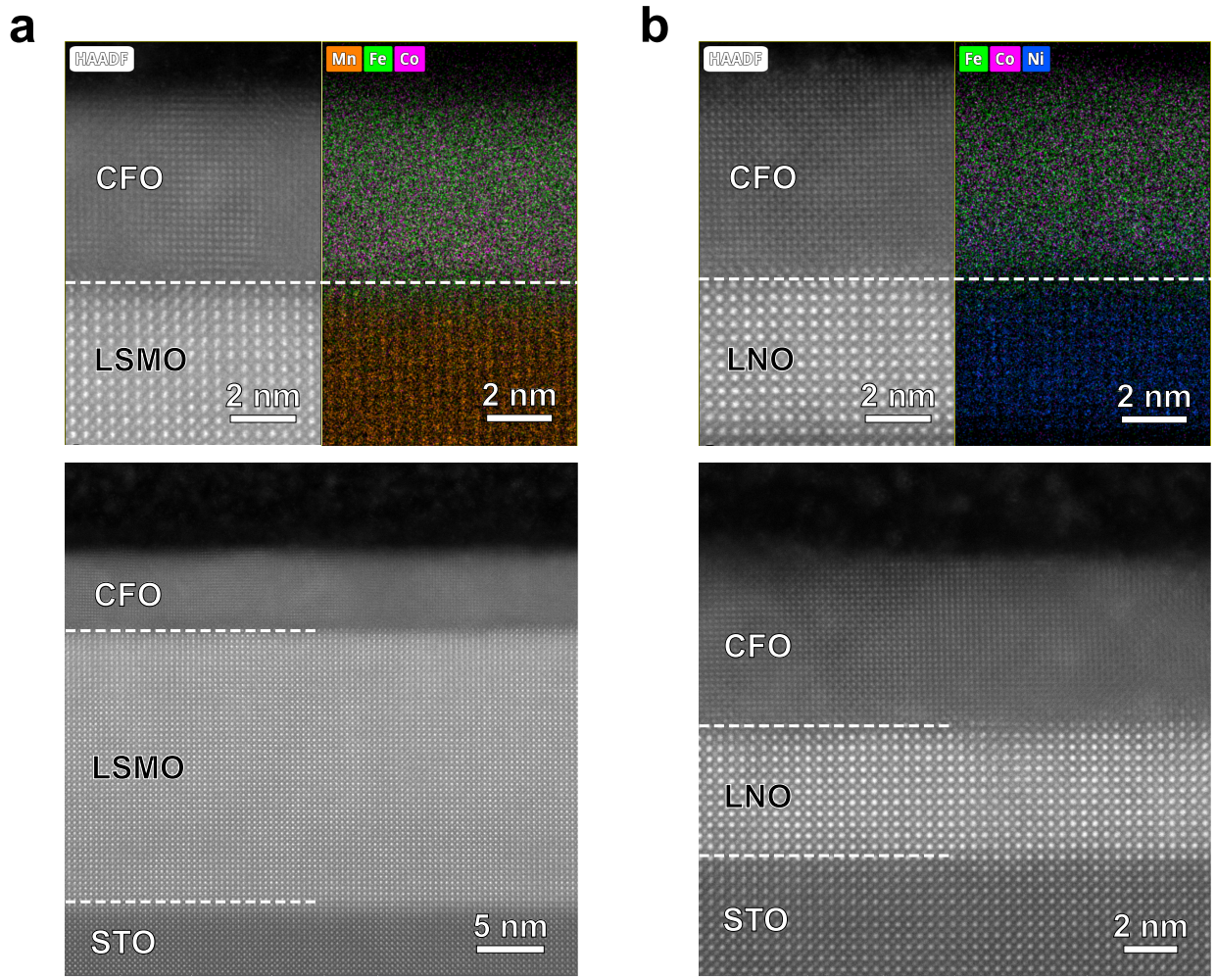

FIGURE S2 HAADF-TEM and EDX analysis of (a) CFO/LSMO and (b) CFO/LNO epitaxial multilayers.

Cross-sectional transmission electron microscopy images reveal uniform and continuous coverage of the perovskite layers (LNO and LSMO) by the top CFO spinel layer in both heterostructures, ensuring that the electrolyte is in contact exclusively with the CFO surface. Energy-dispersive X-ray elemental mapping confirms a homogeneous distribution of transition metals throughout the film thickness, with no detectable interdiffusion or intermixing across the interfaces. Slight differences in the CFO layer atomic pattern between multilayer are caused by the antiphase boundary defects (APB) due to the spinel/perovskite interface.

S.3 RHEED-controlled pulsed-laser deposition of epitaxial multilayers

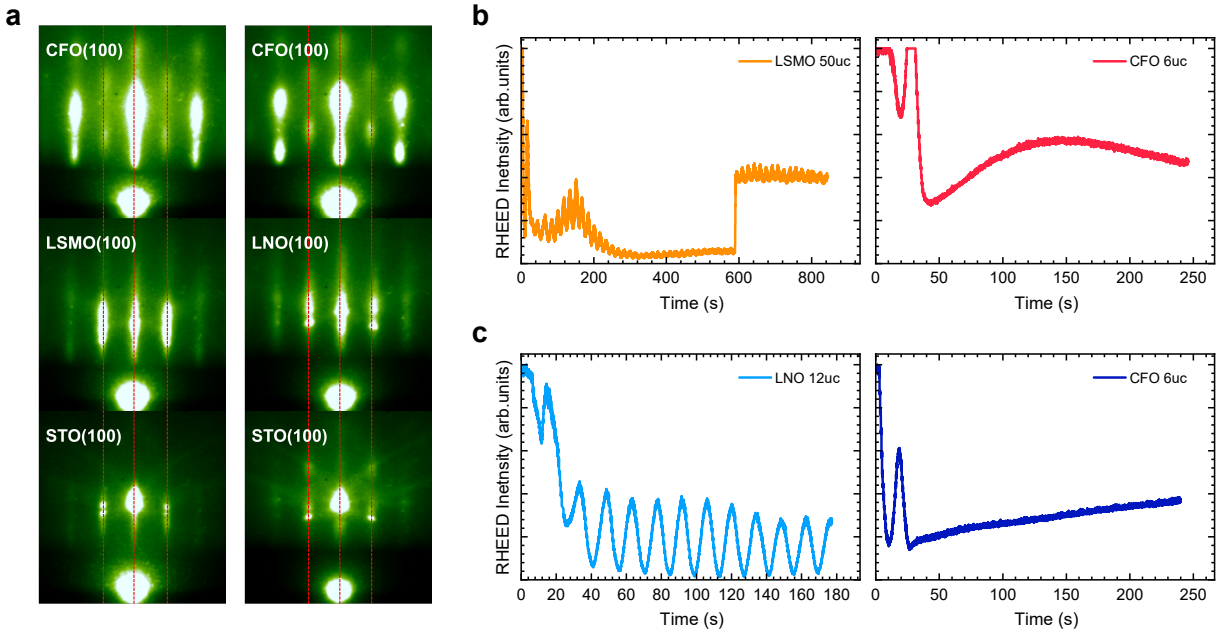

FIGURE S3 (a) RHEED patterns of CFO (6 uc)/LSMO (50 uc) and CFO (6 uc)/LNO (12 uc) multilayers were recorded after the growth of each individual layer. The patterns indicate predominant two-dimensional growth. Red dashed line serves as a visual guidance for distance between diffraction spots of STO perovskite substrate. Time-dependent intensity evolution of the (0,0) RHEED specular spot during the growth of (b) CFO/LSMO and (c) CFO/LNO multilayers. Sudden intensity increase during the LSMO layer growth is due to the manual RHEED current increase.

The diffraction patterns obtained after the deposition of the LNO and LSMO layers are consistent with their perovskite crystal structure, exhibiting the same main diffraction spots as the STO substrate. In contrast, after the growth of the spinel CFO surface layer, the diffraction pattern changes significantly, consistent with an approximately twofold larger lattice parameter compared to the perovskite structure. Time-dependent (0,0) RHEED specular spot intensity evolution of LNO and LSMO perovskite layers clearly shows oscillations that were used to in-situ monitor the film thickness. The top CFO spinel layer does not show any oscillation behavior on both perovskite buffers, which could be explained by a large lattice parameter mismatch between the layers. Therefore, XRR was used to normalise the spinel growth rate prior to the experiment.

S.4 Temperature-dependent magnetization and magnetic hysteresis at 340 K of CFO/LSMO and CFO/LNO multilayers

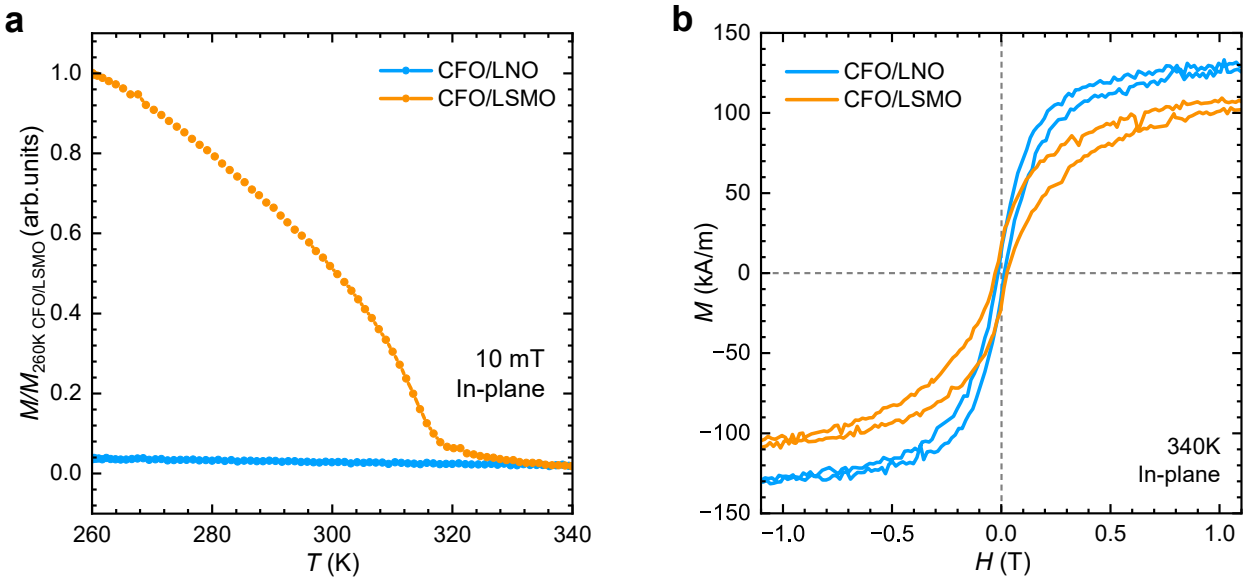

FIGURE S4 (a) CFO (6 uc)/LSMO (50 uc) and CFO (6 uc)/LNO (12 uc) M(T) curves were measured by warming under an in-plane magnetic field of 10 mT and normalized to the magnetization of the CFO/LSMO sample at 260 K. (b) M(H) dependance of CFO-based multilayers at 340 K

The CFO/LSMO multilayers shows a clear ferromagnetic–paramagnetic transition of the LSMO layer at about 318 K, while CFO layer-induced magnetization persists at higher temperatures. In contrast, no magnetic transition is observed for the CFO/LNO due to paramagnetic nature of LNO perovskite with the CFO layer magnetization values at 340 K being comparable to that of CFO/LSMO. Magnetic hysteresis loops at 340 K recorded above the T_C of the LSMO buffer layer show similar behavior for both samples. Small differences likely arise from strain or growth-related effects induced by the underlying perovskite layers. The data after magnetic saturation above 1 T field was linearly fitted and subtracted to remove diamagnetic (STO substrate) and paramagnetic (LNO and LSMO above the Curie temperature) contributions, leaving only CFO hysteresis curve.

S.5 Electrochemical cell for field dependent measurements

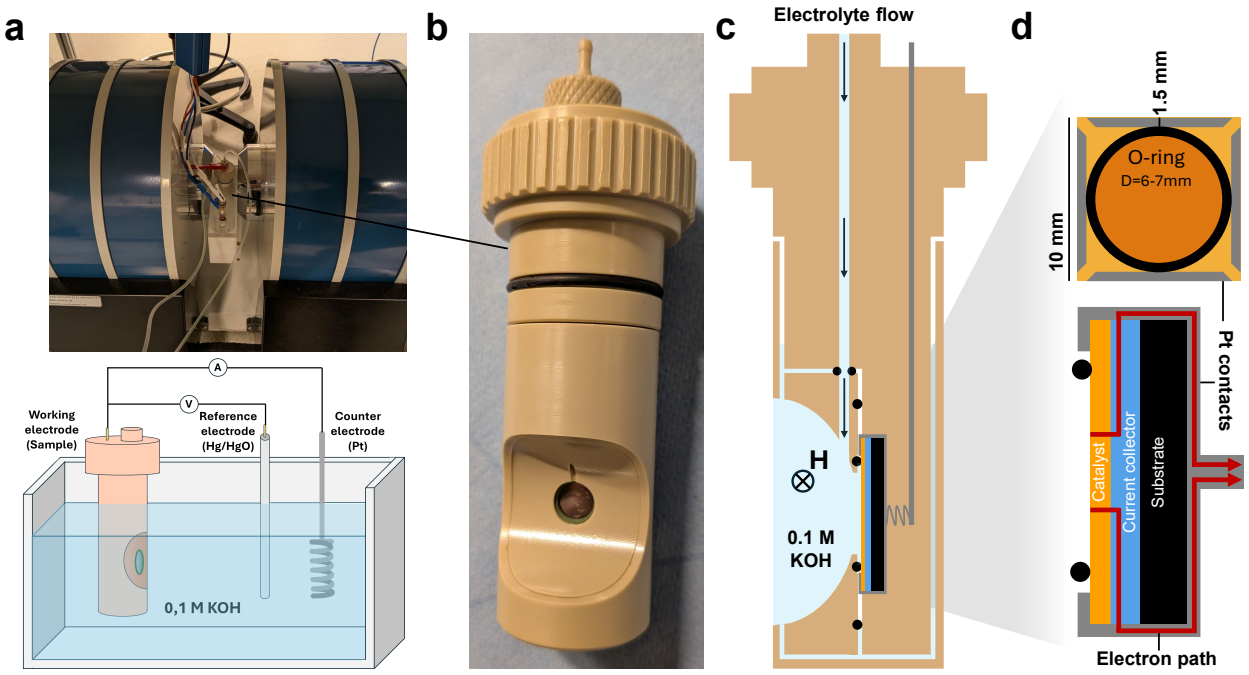

FIGURE S5 (a) Placement of the cell in the electromagnet and the cell schematic: the holder with the sample is positioned in the center of the coils, while the reference and counter electrodes are placed outside the coils. (b) Close-up of the sample holder. The small round area shows the exposed surface of the sample. (c) Schematic side view of the sample holder. The sample is secured by PEEK components and connected via Pt contacts to the external electronics with O-rings preventing electrolyte leakage. An electrolyte flow ensures continuous refreshment of the electrolyte at the sample surface. In-plane direction of the magnetic field relative to the sample is indicated by H. (d) Zoomed in view of the sample within the setup. Top: front view of the sample showing side contacts of Pt sputtered on the front to enable electrical connection to the back contacts and the placement of the O-ring. The area inside the O-ring is exposed to the electrolyte. Bottom: side view indicating the current flow for a sample grown on an insulating substrate.

A custom electrochemical cell was designed to enable measurements under variable magnetic fields. To ensure accurate and reproducible data, the gap between the electromagnet poles was minimized to reduce Joule heating, and potential heating effects of the magnet were considered in data interpretation; however, these effects could not account for the observed trends. Only the working electrode (WE) was positioned within the high-field region, while the counter electrode (CE), reference electrode (RE), and all wiring were kept outside the magnet center. As a result, with a maximum field of 1 T on the working electrode that was used in this work for electrochemical characterization, magnetic fields on the counter and reference electrodes were 0.4 T and 0.25 T, respectively. Additionally, by employing a flow cell configuration with a liquid flow of 0.27 ml/s that continuously replaced the electrolyte at the catalyst interface, we minimized uncontrolled mass transport effects arising from the interplay between natural electrochemical transport and magnetohydrodynamic (MHD) flows.

S.6 Magnetoresistance measurements

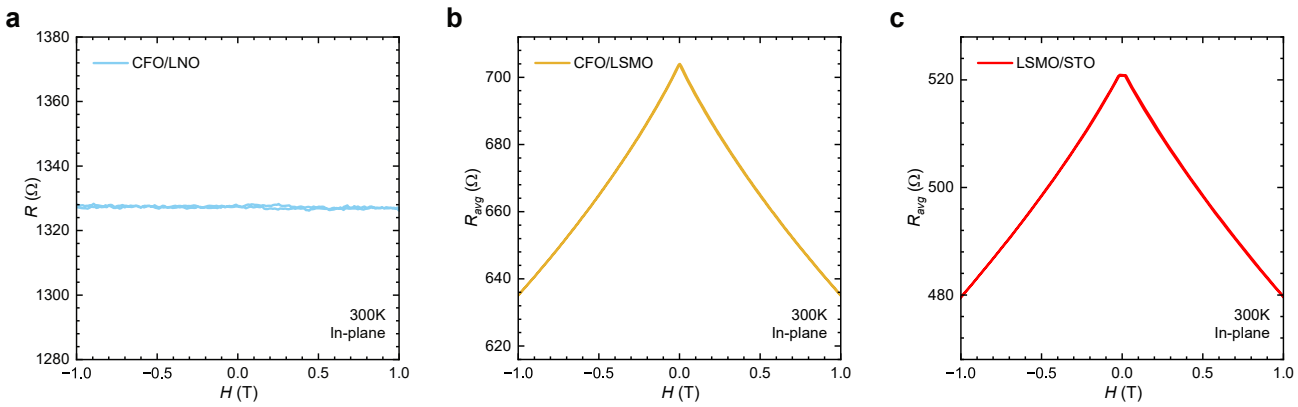

FIGURE S6 (a) Two-point Resistance measurements of (a) CFO (6 uc)/LNO (12 uc) and average resistance measurements of (b) CFO (6 uc)/LSMO (50 uc) multilayers and a bare LSMO (50 uc) reference as a function of in-plane magnetic fields at 300 K, revealing magnetoresistive effects in samples incorporating a ferromagnetic current collector..

MR measurements for the CFO/LNO multilayer reveal no dependence of the two-point resistance on the applied magnetic field, while the CFO/LSMO multilayer clearly shows negative MR behavior (Figure S6a). Moreover, the decrease in the sheet resistance for CFO/LSMO with an increasing magnetic field shows a similar trend compared to bare LSMO/STO films, clearly pinpointing LSMO as the origin of the effect (Figure S6b,c). Differences in the MR behavior are attributed to the insulating CFO top layer present in the multilayers.

S.7 Demonstration of the magnetic enhancement effect on multilayer with 20 nm CFO top surface

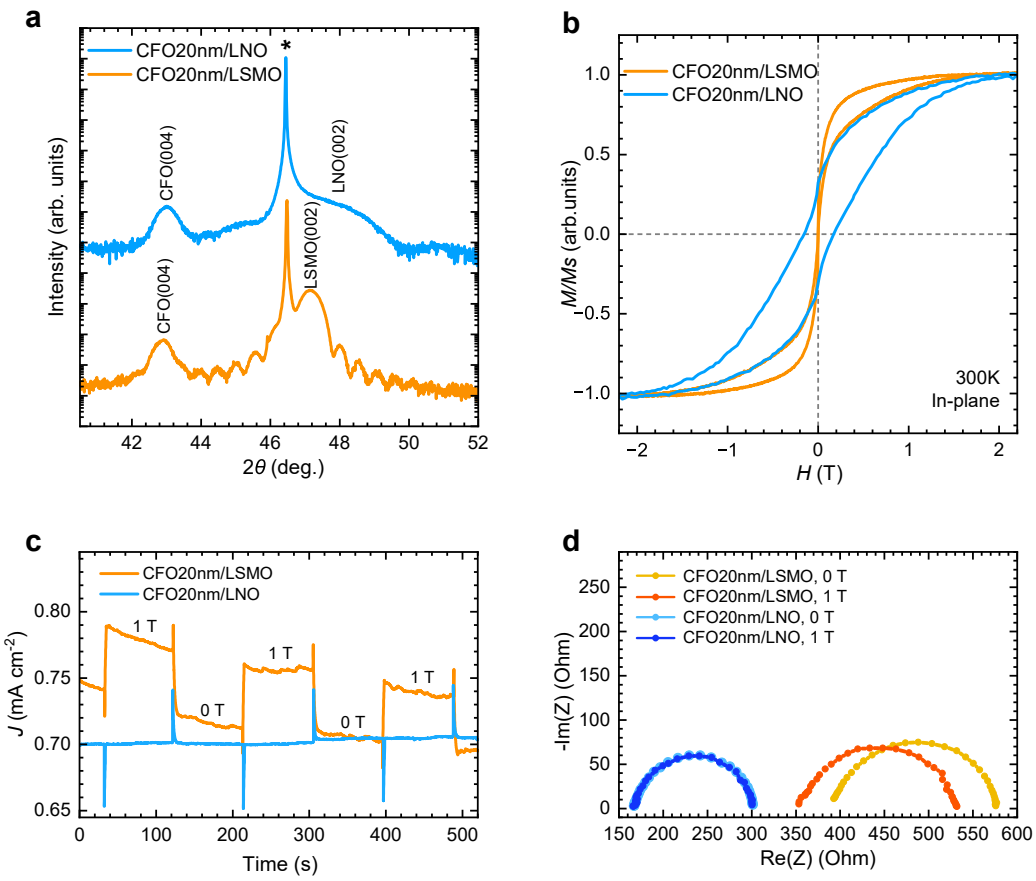

FIGURE S7 (a) Out-of-plane XRD θ–2θ scans, (b) magnetic hysteresis loops,(c) CA and (d) PEIS analysis of epitaxial multilayers with 20 nm CFO top surface. Note that the CFO20nm/LNO (12 uc) impedance data at 0 T and 1 T almost completely overlaps. PEIS data was recorded at 1.71 V vs RHE (CFO20nm/LSMO) and 1.65 V vs RHE (CFO20nm/LNO) to reach the OER current density of approximately 0.7 mA/cm^2.

XRD analysis clearly shows more pronounced CFO(004) peaks compared to the XRD scans of multilayers with 5 nm CFO surface shown in the main text, confirming increased thickness of the top layer. Magnetic hysteresis loops also show clear changes. The CFO (20 nm)/LNO multilayer exhibits a more coercive hysteresis loop, with the coercive field increasing to approximately 170 mT, resembling the typical magnetic behavior of CFO. For the CFO (20 nm)/LSMO (50 uc) multilayer, a widening of the hysteresis at higher fields—where the LSMO layer is already magnetically saturated—is observed, indicating a similar increase in the coercivity of the CFO layer in this heterostructure. Despite these changes in the samples properties, the CA and PEIS analysis show the same observations as for the 5 nm CFO samples, demonstrating no dependence of the OER enhancement on the top layer magnetic properties and once again reaffirming the MR origin of the magnetic enhancement effect.

S.8 Magnetic enhancement effect during the methanol oxidation reaction (MOR)

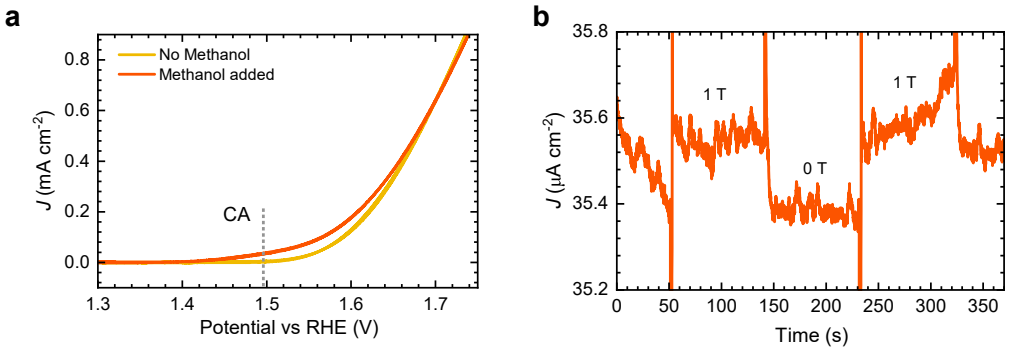

FIGURE S8 (a) CV curves of CFO (20 nm)/LSMO (50 uc) multilayer in 0.1 M KOH solution before and after methanol addition. (b) CA analysis at 1.498 V vs RHE with and without 1 T external magnetic field.

The methanol oxidation reaction (MOR) and the OER can be performed on the same electrode but differ fundamentally in their reaction pathways and kinetic constraints. While MOR involves spin-independent oxidation of an organic molecule and primarily probes charge-transfer and mass-transport properties, OER involves a spin-selective O–O bond formation. The spin-selectivity of OER should therefore not be observable in MOR, while the MR affects both reactions equally. We compare the activity of 20 nm CFO layers on LSMO with and without addition of 1 ml methanol per 100 ml of KOH solution. CV analysis clearly shows an increased current density at low potentials after the addition of methanol, consistent with the lower oxidation potential of methanol compared to oxygen. CA analysis below the OER onset potential shows a small current density increase in the 1 T magnetic field, which disappears with the field removal. We note that MR effects increase with the overall current, therefore the enhancement in the MOR are smaller than the OER enhancements at high currents shown in the main text. This experiment thus reveals a magnetic enhancement effect in the MOR reaction, despite only diamagnetic species participating in it.

S.9 Determination of uncompensated resistance for CP calculations

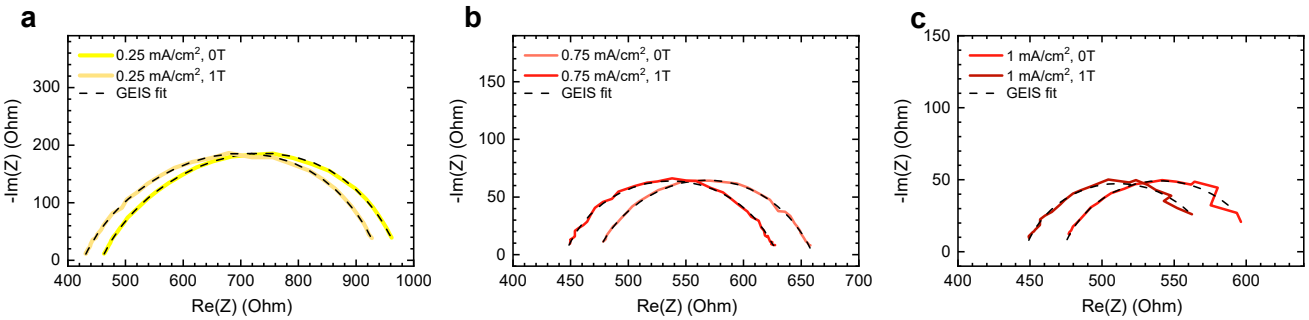

FIGURE S9 (a) 0.25 mA/cm^2, (b) 0.75 mA/cm^2 and (c) 1 mA/cm^2 GEIS experimental data and fitted curves.

Fitting of GEIS was performed using an Ru-RC-RQ equivalent circuit as described in the main text, where R_u part was used to determine uncompensated resistance and, therefore, resistance change upon magnetic field application for the CP calculations. For GEIS measurements done at current densities of 0.25 mA/cm2, 0.75 mA/cm2 and 1 mA/cm2, ΔR_u values after fitting were found to be 31.8 Ohm, 27.6 Ohm and 26.17 Ohm, respectively.These values were used for the CP calculations given in Figure 3 of the main text. The decrease in uncompensated resistance for different current densities could be explained by bubble formation at the surface contributing at higher current densities and at progressively longer exposure time to OER conditions.

S.10 Limitations of the chronopotentiometry calculations

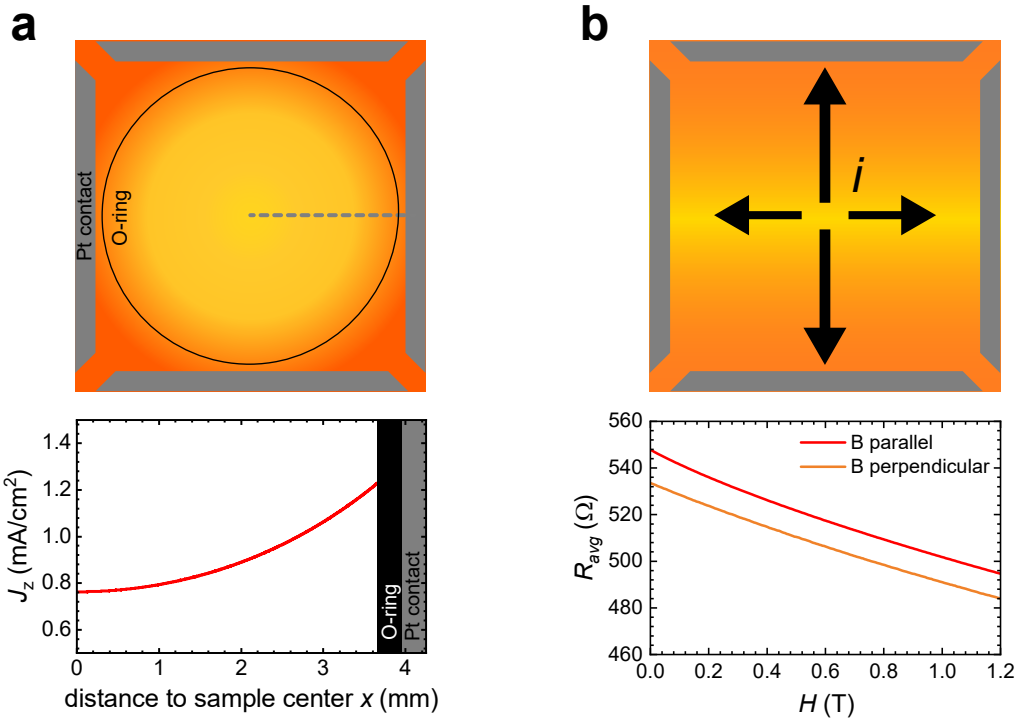

FIGURE S10 (a) Top: Schematic illustration of spatially inhomogeneous OER activity across the sample surface, arising from a lateral gradient in uncompensated resistance toward the Pt side contacts. Regions farthest from the contacts (lighter color) exhibit the highest resistance and therefore reduced electrochemical activity under an applied potential, whereas regions closer to the contacts (darker color) experience lower resistance and enhanced activity. Bottom: Simulated current-density distribution along the dotted line for LSMO thin films on an insulating substrate. Simulations were performed as described in [1]. (b) Top: Illustration of current-density inhomogeneity induced by anisotropic resistance effects, such as anisotropic magnetoresistance or anisotropic in-plane resistance due to magnetic anisotropy caused by miscut-induced surface steps, crystal anisotropy or anisotropic strain. Bottom: Resistance anisotropy as a function of the relative orientation between the current direction and the magnetization (or applied magnetic field), measured while sweeping the magnetic field from 1.2 T down to 0 T. When the magnetization/field is parallel (perpendicular) to the current, the resistance is higher (lower), consistent with AMR behavior. However, the magnitude of this effect is small for the thin films used in this study, with a maximum resistance difference of only $\sim$10 Ω, corresponding to about 2%. Owing to resistance anisotropy along the [001] and [010] directions, R_{avg} is defined as the average of the resistances measured along these axis, taken separately for magnetic fields applied parallel and perpendicular to the current.

As shown in the main text, the comparison of the experimental ΔE values with $i\Delta R_u$ calculations reveals similar trends, but not a complete overlap. One possible explanation for this discrepancy is the presence of inhomogeneous current pathways, which generate spatial variations in the effective R_u (Fig. S10a). Because R_u increases from the edge toward the center, the magnetoresistance effect is strongest in the central regions. This affects ΔE, which reflects the integrated response of all local current paths, whereas $i\Delta R_u$ represents only an averaged resistance change. As a result, $i\Delta R_u$ systematically underestimates the potential drop across the electrolyte-exposed area. This interpretation is supported by the smaller change in R_u compared with the change in the average resistance under the same magnetic field (Fig. 4g, middle panel, main text), indicating that R_u underestimates contributions from certain active regions.

A further source of discrepancy may arise from current-density inhomogeneities resulting from anisotropic resistance within the thin films, such as anisotropic magnetoresistance [2] or anisotropic in-plane resistance due to magnetic anisotropy caused by miscut-induced surface steps [3], anisotropic strain [4,5] or lifting of in-plane lattice degeneracy [6]. Lastly small differences in thickness due to PLD growth could lead to inhomogeneous resistance. Such spatially non-uniform resistance variations partially violate the constant-current assumption used in our CP calculations, contributing to the observed differences between calculated and

experimental potential decrease (Fig. S10b). These effects are expected to be less pronounced in particle-based catalysts or thick films on conductive substrates, where out-of-plane transport dominates, resistances are more homogeneous, and current paths are more randomized.

S.11 Characterization of LCO/LSMO and LFO/LSMO multilayers

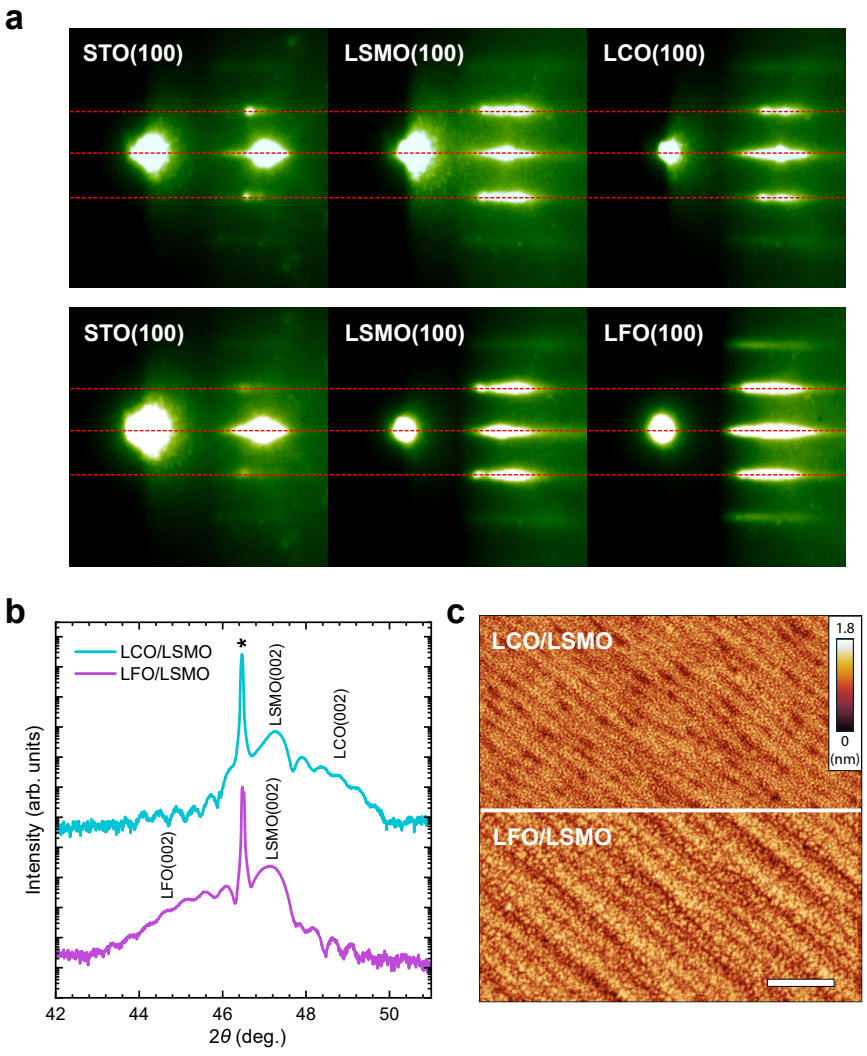

FIGURE S11 (a) RHEED patterns of LCO (12 uc) /LSMO (50 uc) and LFO(12 uc)/LSMO (50 uc) multilayers were recorded after the growth of each individual layer. The patterns indicate two-dimensional growth and are consistent with the perovskite crystal structure, exhibiting the same main diffraction spots as the STO substrate. Red dashed line serves as a visual guidance for distance between diffraction spots of STO perovskite substrate. (b) Out-of-plane XRD θ–2θ scans demonstrate epitaxial growth of all layers in the [001] direction. (c) AFM scans demonstrate full coverage of the LSMO layers by the top surface as well as comparable surface morphology and low roughness between multilayers (scalebar, 500 nm).

S.12 Structural and morphological characterization of LSMO films

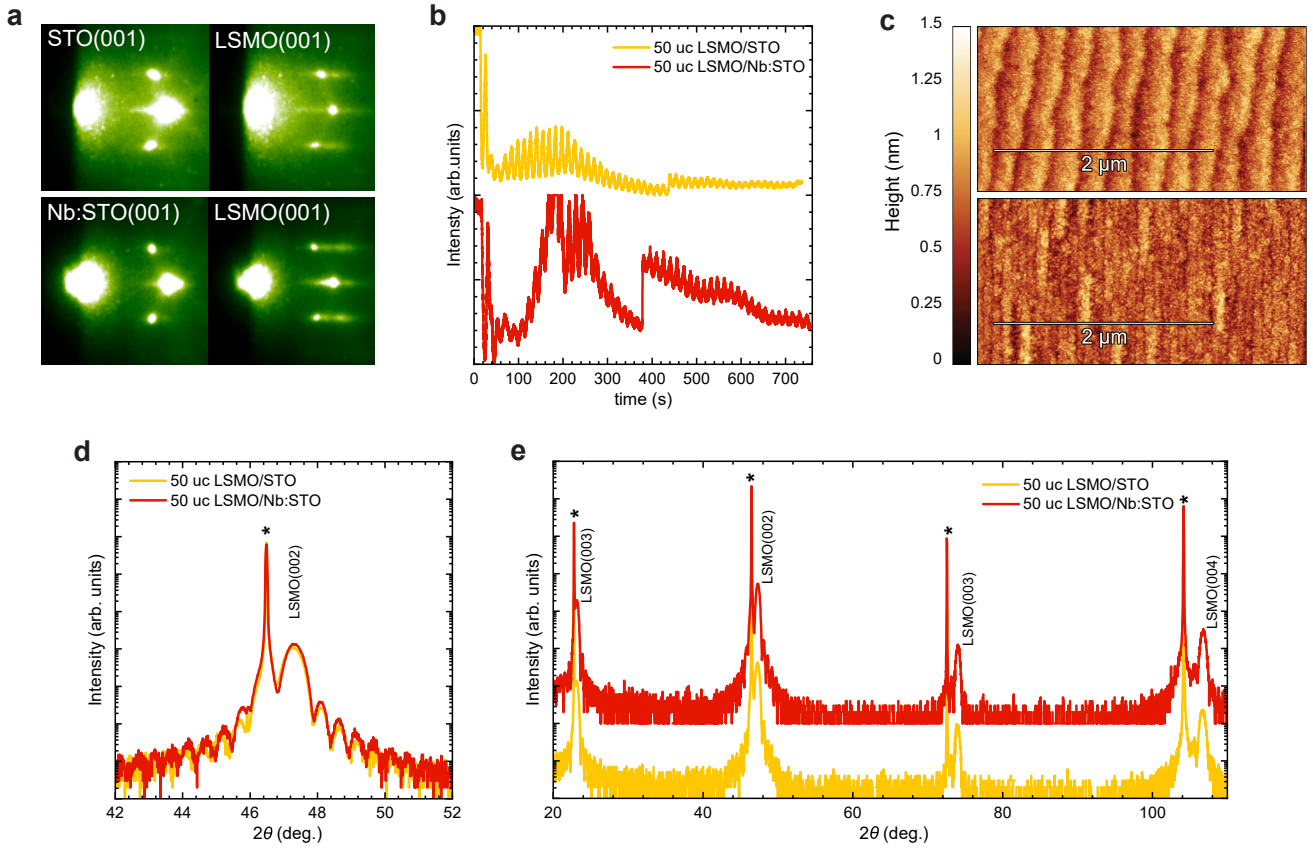

FIGURE S12 (a) RHEED patterns obtained before and after the growth of LSMO (50 uc) grown on STO and Nb:STO substrates. (b) RHEED intensity osscilations during the growth of LSMO. The sudden increases and decreases in intensity was caused by manual change of RHEED currents. (c) AFM images of the LSMO films on both substrates. (d) 2Θ-ω XRD scan of the substrate and thin-film 002 peaks, indicating excellent bulk crystalline quality and consistent out-of-plane lattice constants and thicknesses. (e) 2Θ-ω XRD scan of the substrate and thin-film 001 till 004 peaks, indicating single (001)-oriented $La_{0.67}Sr_{0.33}MnO_3$.

S.13 Background normalization of CA data for LSMO films

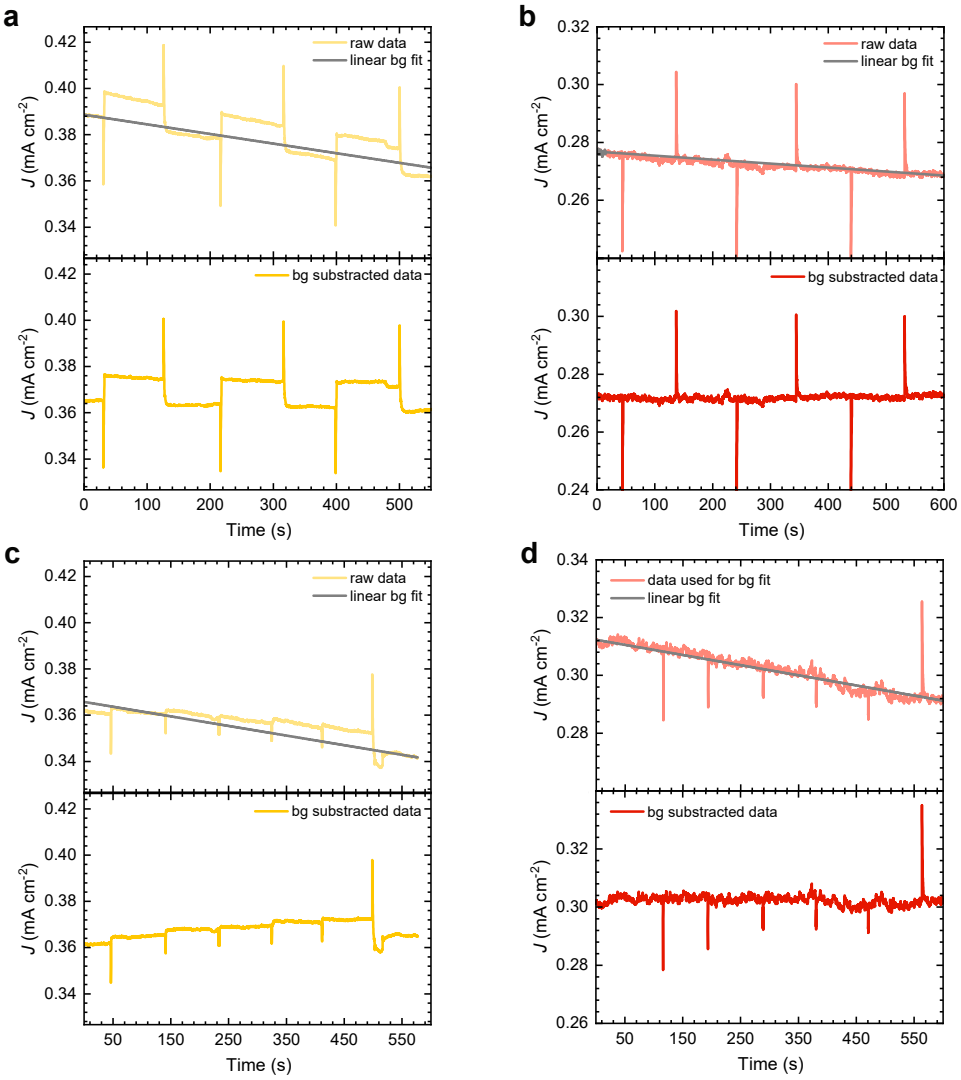

FIGURE S13 (a,b) Raw and background-subtracted chronoamperometry data during 1 T measurements for LSMO (50 uc) on (a) STO and (b) Nb:STO, including the removed linear background. (c,d) Raw and background-subtracted chronoamperometry data during measurements with magnetic-field steps of 0.2 T for the same films on (c) STO and (d) Nb:STO, including the removed linear background.

We observed that the activity of LSMO decreased or increased slightly even after extended potential holds, necessitating a linear background removal to visualize the comparably small changes with applied field. This behavior may originate from surface reconstruction, Sr leaching, or slight corrosion of the samples during operation. To accommodate for those effects, the background subtraction is performed by fitting a linear function to the data before and after the magnetic-field measurements. The fitted linear backgrounds for the data shown in the main text, as well as the signals after background subtraction, are presented in Supplementary Figure S13.

S.14 Impedance characterization and fitting for LSMO films

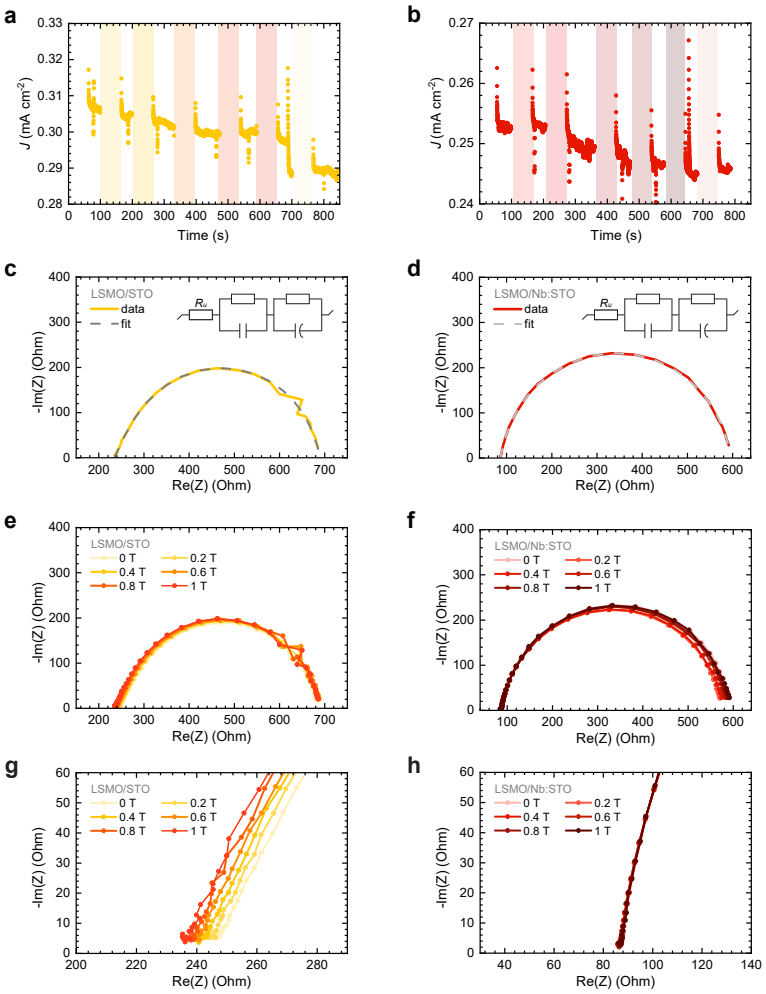

FIGURE S14 (a,b) Chronoamperometry measurements under different magnetic fields, during which in situ PEIS was recorded for LSMO (50 uc) films on (a) STO and (b) Nb:STO at 1.79 V vs RHE (STO) and 1.76 V vs RHE (Nb:STO). The shaded regions indicate the time during which PEIS was performed at the fields corresponding to these colours as seen in respectively g and f. (c,d) Representative PEIS fit for measurements done during the CA measurement for films on (c) STO and (d) Nb:STO. The fits are obtained using an R–RC–RQ equivalent circuit (inset). (e,f) Nyquist plots obtained by PEIS at OER-relevant potentials under the applied fields for films on (e) STO and (f) Nb:STO. The apparent change in R_{ct} in f is attributed to the minor decay in LSMO activity with time, even after extended potential holds, as discussed in the previous section. This behavior is also evident in panel b, where a continuous decrease in the total current density can be observed. (g,h) Zoom in on R_u of panels e and f.

S.15 Impact of Magnetoresistance on OER in High-Resistance LSMO Films

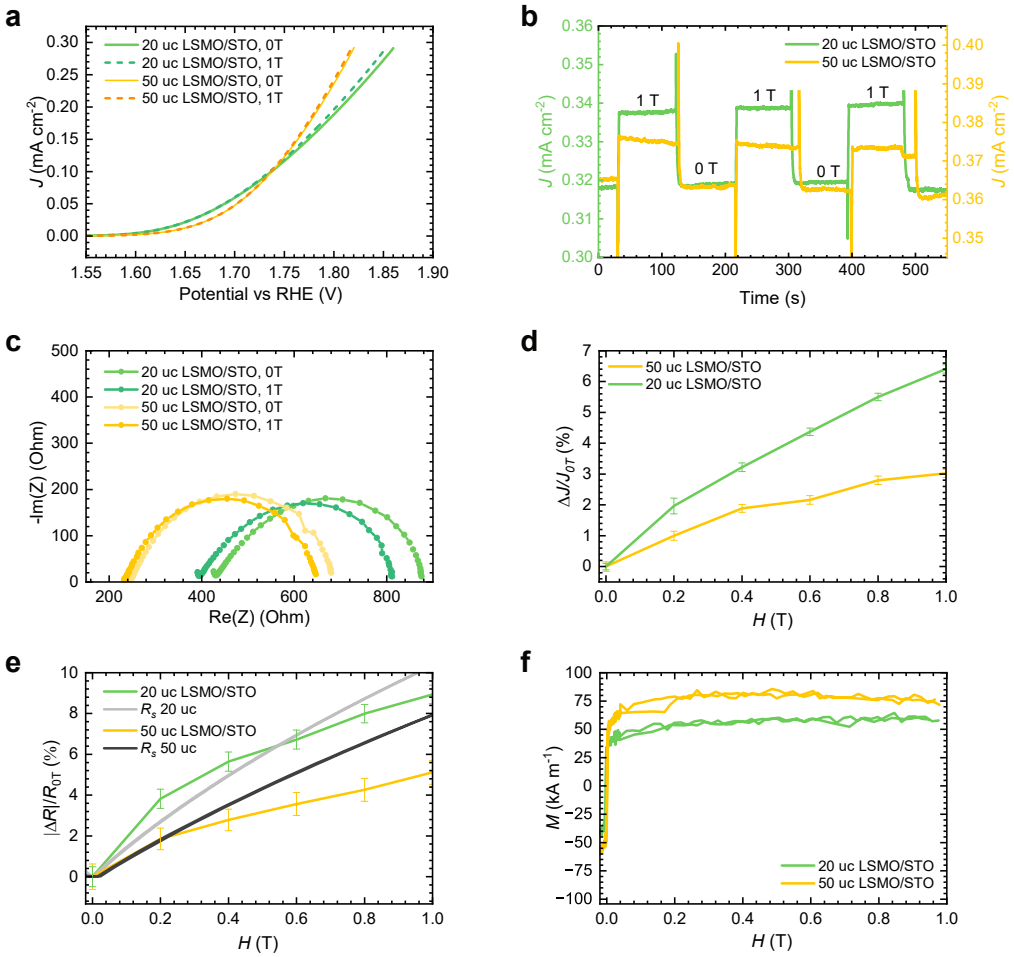

FIGURE S15 (a) Cyclic voltammograms of 20 and 50 uc thick LSMO films grown on STO under 0 and 1 T fields. (b) Nyquist plots from PEIS during chronoamperometry at OER-relevant potentials, at 1 T and 0 T. (c) Chronoamperometry measurement of the LSMO films at 1.79 V (50 uc) and 1.70 V (20 uc) vs. RHE, during which the field was changed from 0T to 1T and back. A linear background was subtracted to remove surface-related current decay. (d) Relative changes in current density. (e) Relative change in uncompensated resistance together with the magnetic-field-dependent sheet resistance. (f) Volume magnetization of the films. All quantities in d-f are plotted as a function of the applied magnetic field.

Repeating the electrochemical measurements on a 20 uc thick LSMO film, with similar structural properties and comparable volume magnetization (Figure S15f) but a higher intrinsic resistance (Figure S15e), results in a more pronounced magnetic-field-induced increase in current density in both CV and CA, accompanied by larger changes in the uncompensated resistance (Figures S15a,b,c). Furthermore, comparing the relative changes in uncompensated resistance and magnetic-field-dependent sheet resistance with the relative changes in current density (Figures S15d,e) reveals the same trend observed in the main text: the relative change in current density closely follows the behavior of the resistances. In contrast, the magnetization exhibits a completely different behavior (Figure S15f). These results again confirm that magnetoresistance is the sole origin of the OER current-density changes under an applied magnetic field. A distinction from the main text, however, is that here the difference between R_u and R_s is smaller.

S.16 Correlation of catalytic current increase with the MR effect and magnetization saturation in CFO-based multilayers

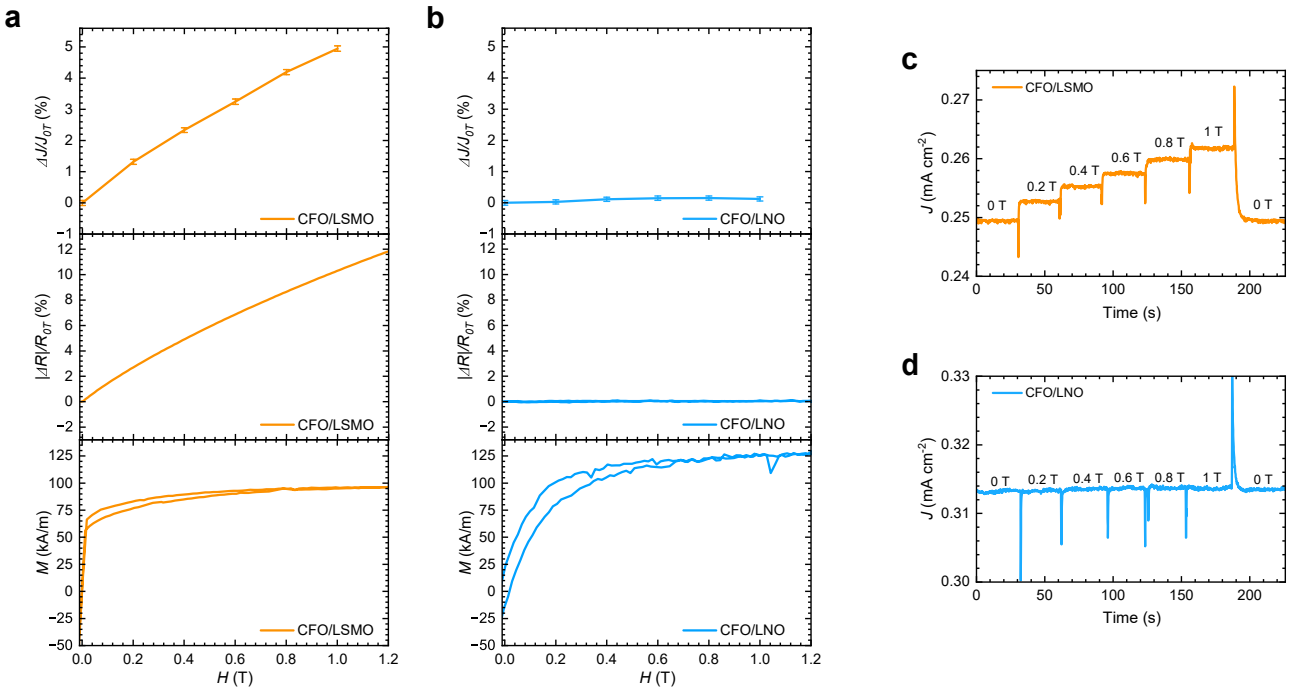

FIGURE S16 Direct comparison of catalytic current increase, saturation magnetization and electrical resistance from applied magnetic field in (a) CFO (6 uc)/LSMO (50 uc) and (b) CFO (6 uc)/LNO (12 uc) multilayers. MR data is plotted as the value of resistance difference at certain magnetic field and at 0 T divided by resistance value at 0 T. For ease of comparison, the absolute value of ΔR is used. However, the actual value is negative due to the presence of negative magnetoresistance. Magnetic enhancement of OER in (a) CFO/LSMO and (b) CFO/LNO multilayers under several applied magnetic fields.

Comparison of catalytic current increase in applied magnetic field with saturation magnetization (M_s) changes under similar fields reveals no correlations. Both multilayers demonstrate minimal changes of the M_s after 0.4 T, while a clear rise in the OER activity could still be observed at higher fields for CFO/LSMO multilayer. Contrarily, no current increase is observed for CFO/LNO heterostructure, despite a clear magnetic hysteresis being present. However, the trend in the OER current increase with increasing magnetic field clearly matches that of electrical resistance changes, connecting magnetic enhancement and MR effects. The percentage-increase in OER current was calculated by performing chronoamperometry under several applied magnetic fields. After applying the field, electrochemical measurement was stabilized to ensure its stability and then the average current value for each step was found.

S.17 MOKE and VSM comparison

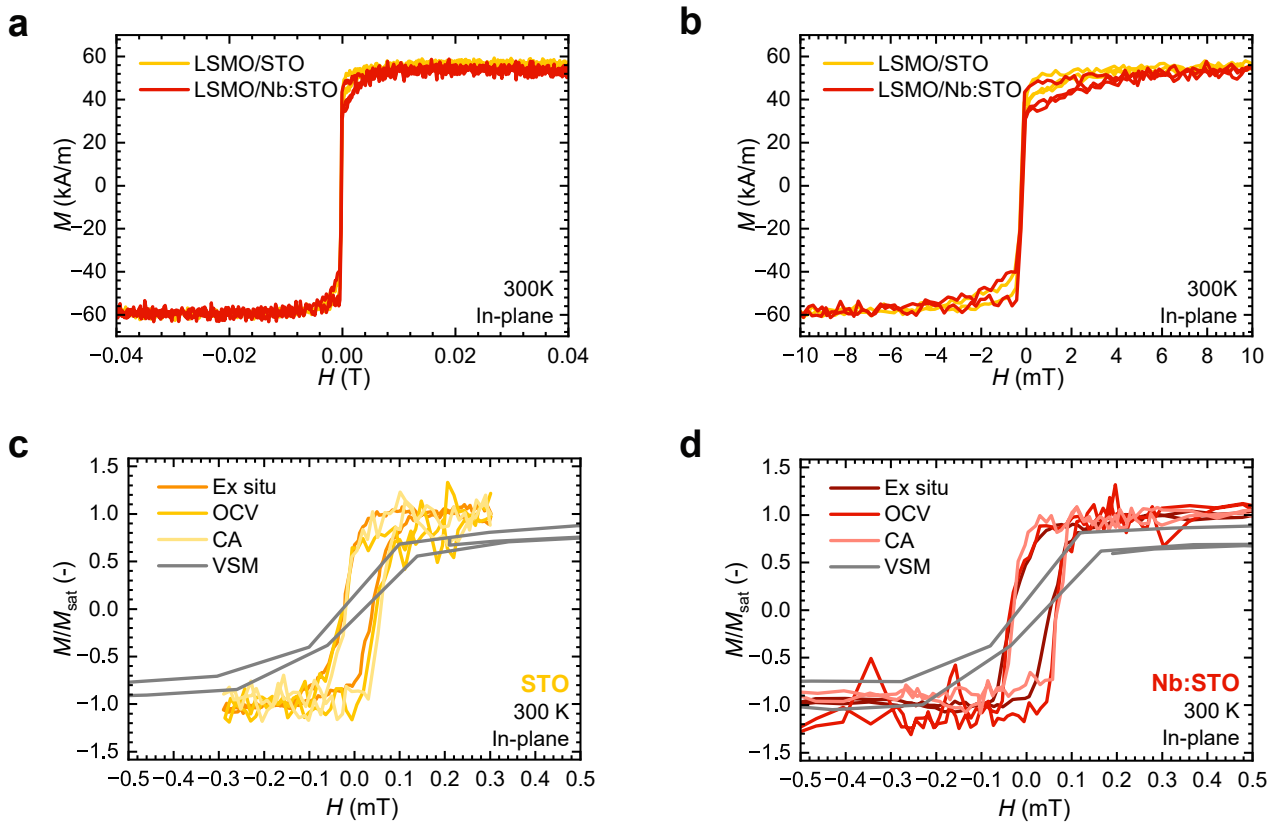

FIGURE S17 (a, b) Zoomed views of the VSM signal for LSMO (50 uc) films on STO and Nb:STO. Comparison of hysteresis loops measured by MOKE and VSM for the same films on (c) STO and (d) Nb:STO. The limited number of data points in the VSM data in this field range arises from PPMS system sensitivity.

S.18 PLD growth parameters

TABLE S1 PLD deposition parameters

Film	Temperature [°C]	Laser fluence [J cm^{-2}]	Frequency [Hz]	O_2 pressure [mbar]
$CoFe_2O_4$	450	3	2	0.05
LSMO	750	1.9	2	0.2
$LaNiO_3$	450	1.8	2	0.04
$LaFeO_3$	670	1.9	2	0.01
$LaCoO_3$	670	1.8	2	0.1

S.19 Electrochemical cell for MOKE measurements

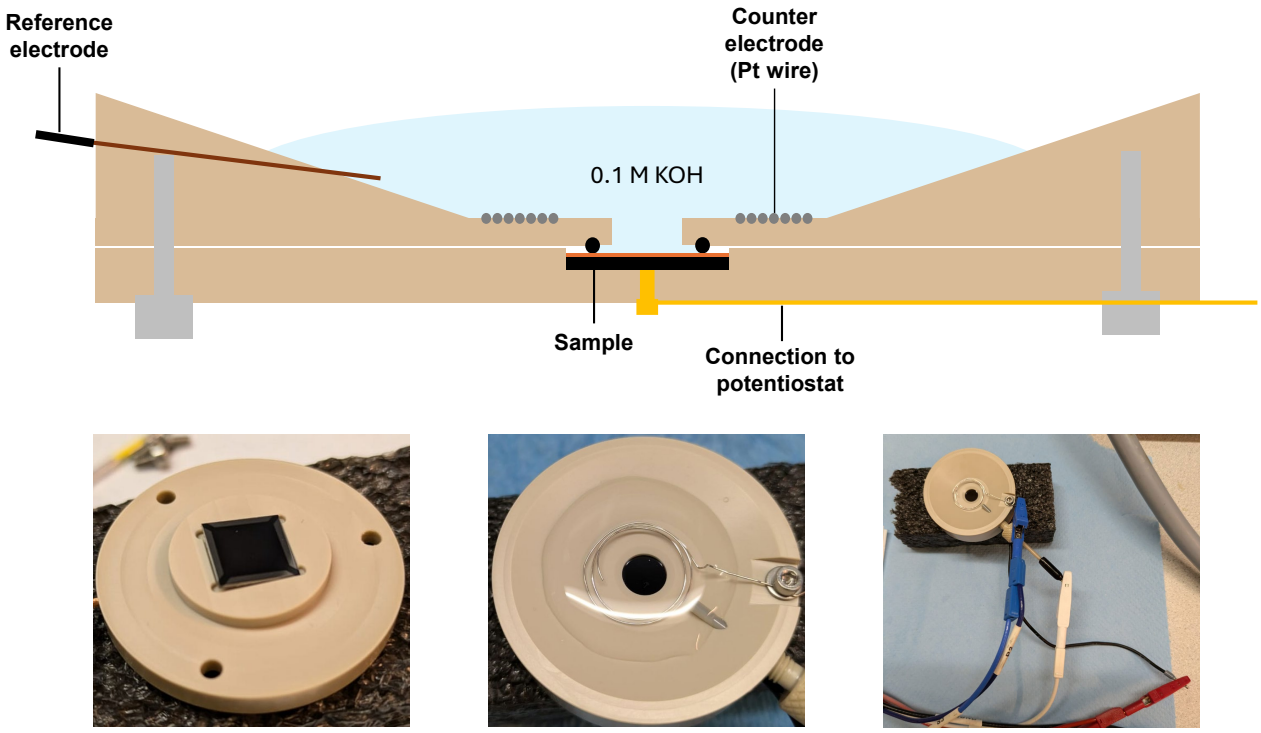

FIGURE S18 Top: Schematic side view of the cell. The sample is secured by PEEK components and an O-ring and connected via copper contacts to the external electronics. Around the exposed area the counter electrode lies to make sure it does not block the view on the sample but is close. Bottom: Pictures of the cell. The small round area shows the exposed surface of the sample.

A custom electrochemical cell was designed to enable *operando* MOKE microscopy measurements during electrochemical experiments. For this purpose, a three-electrode cell with an open-top configuration was developed. Ag/AgCl leakless electrode was used as reference electrode, while Pt wire around the sample served as a counter electrode.

REFERENCES

1. Heymann L, Bosch v. dICG, Wielens DH, et al. Revealing the Intrinsic Oxygen Evolution Reaction Activity of Perovskite Oxides across Conductivity Ranges Using Thin Film Model Systems. *ACS Applied Materials & Interfaces.* 2025;17(14):21110–21121. doi: 10.1021/acsami.4c20141
2. Coey J. *Magnetism and Magnetic Materials*:128–194; Cambridge University Press . 2001
3. Mathews M, Postma FM, Lodder JC, Jansen R, Rijnders G, Blank DHA. Step-induced uniaxial magnetic anisotropy of $La_{0.67}Sr_{0.33}MnO_3$ thin films. *Applied Physics Letters.* 2005;87(24). doi: 10.1063/1.2143136
4. Liao Z, Huijben M, Koster G, Rijnders G. Uniaxial magnetic anisotropy induced low field anomalous anisotropic magnetoresistance in manganite thin films. *APL MATERIALS.* 2014;2(9). doi: 10.1063/1.4895956
5. Gong J, Zheng D, Li D, Jin C, Bai H. Lattice distortion modified anisotropic magnetoresistance in epitaxial $La_{0.67}Sr_{0.33}MnO_3$ thin films. *Journal of Alloys and Compounds.* 2018;735:1152–1157. doi: 10.1016/j.jallcom.2017.11.221
6. Boschker H, Mathews M, Brinks P, et al. Uniaxial contribution to the magnetic anisotropy of $La_{0.67}Sr_{0.33}MnO_3$ thin films induced by orthorhombic crystal structure. *Journal of Magnetism and Magnetic Materials.* 2011;323(21):2632–2638. doi: 10.1016/j.jmmm.2011.05.051